The South Pacific Pressure Trend Dipole and the Southern Blob

René D. Garreaud[1,*], Kyle Clem[2] and José Miguel Vicencio[3]

(1) Department of Geophysics, Universidad de Chile, Santiago, Chile

(2) School of Geography, Environment and Earth Sciences; Victoria University of Wellington, New Zealand

(3) Climatología, Dirección Meteorológica de Chile, Santiago, Chile

(*) Corresponding author:

René D. Garreaud

Department of Geophysics, Universidad de Chile

Blanco Encalada 2002, Santiago, CHILE

E-mail: rgarreau@dgf.uchile.cl

Abstract

During the last four decades, the sea level pressure has been decreasing over the Amundsen-Bellingshausen Sea (ABS) region and increasing between 30-40°S from New Zealand to Chile, thus forming a pressure trend dipole across the South Pacific. The trends are strongest in austral winter and have influenced the climate of West Antarctica and South America. The pressure trends have been attributed to decadal variability in the tropics, expansion of the Hadley cell and an associated positive trend of the Southern Annular Mode, but these mechanisms explain only about half of the pressure trend dipole intensity. Experiments conducted with two atmospheric models indicate that upper ocean warming over the subtropical southwest Pacific (SSWP), termed the Southern Blob, accounts for about half of the negative pressure trend in the ABS region and nearly all the ridging /drying over the eastern subtropical South Pacific, thus contributing to the central Chile megadrought. The SSWP warming intensifies the pressure trend dipole through warming the troposphere across the sub-tropical South Pacific and shifting the mid-latitude storm track poleward into the ABS. Multi-decadal periods of strong SSWP warming also appears in fully coupled pre-industrial simulations, associated with a pressure trend dipole and reduction in rainfall over the central tropical Pacific, thus suggesting a natural origin of the Southern Blob and its teleconnection. However, the current warming rate exceeds the range of natural variability, implying a likely additional anthropogenic contribution.

1. Introduction

The atmospheric circulation over the extratropical South Pacific exhibits strong variability at interannual and interdecadal timescales (Connolley 1997; Fogt et al. 2012). This is due in part to the Antarctic topography and the off-axis orientation of Antarctica about the pole by which variations in the westerly wind strength leads to strong fluctuations in pressure over the South Pacific (Baines and Fraedrich 1989; Lachlan-Cope et al. 2001), as well as strong teleconnections stemming from tropical sea surface temperature (SST) anomalies (Lachlan-Cope and Connolley 2006; Ding et al. 2012; Clem et al. 2017a). Early studies focused on year-to-year variability and identified the Pacific South America (PSA) mode (Mo and Ghil 1987; Kidson 1988; Lau et al. 1994), a well-defined wave train with three circulation nodes arching from the western tropical Pacific to Argentina with major impacts on the climate of South America and Antarctica (e.g., Montecinos et al. 2000; Irving and Simmonds, 2016). The PSA was subsequently linked to SST anomalies in the equatorial Pacific occurring during El Niño Southern Oscillation (ENSO) events (e.g., Karoly 1989) although a PSA-like pattern can also be excited by the Madden-Julian Oscillation at intraseasonal timescales (Flatau and Kim 2013; Henderson and Maloney 2018; Lee and Seo 2019).

Recently, attention has been placed on the pressure decline in the periphery of West Antarctica during the last 3-4 decades (e.g., Jones et al. 2016; Raphael et al. 2016). We refer to this region as the Amundsen-Bellingshausen Sea (ABS: 70°-60°S; 230°-280°E, see box in Fig. 1a). In particular, the deepening of the Amundsen Sea Low (ASL) has been linked with observed sea ice trends in the South Pacific (Stammerjohn et al. 2012; Purich et al. 2016; Meehl et al. 2016) and surface warming across West Antarctica (Ding and Steig 2013; Clem and Fogt 2015;

Bromwich et al. 2012). Idealized numerical experiments have found the recent deepening is largely linked to SST anomalies from a variety of tropical sources including the tropical Pacific, Atlantic and Indian oceans (Li et al. 2014; Ding et al. 2012). The strength of these teleconnections varies seasonally, in part because of the seasonal variability in the subtropical jet over Australia and the adjacent South Pacific which interferes with Rossby wave propagation from the tropics into higher latitudes (Li et al. 2015; Yiu and Maycock 2019). The position and intensity of the ASL is also modulated by the Southern Annular Mode (SAM; e.g., Fogt et al. 2012). The SAM trend towards its positive polarity during austral summer due to ozone depletion thus emerge as another important driver of the ASL deepening in summer (e.g., England et al. 2016), while tropical variability is a more important driver of the ASL deepening in autumn (Ding and Steig 2013) and spring (Clem and Fogt 2015). Recent modelling studies suggest that cooling of the eastern equatorial Pacific from 2000 to 2014 was the primary forcing of the negative sea level pressure (SLP) anomalies over the ABS region in this period (Trenberth et al. 2014; Meehl et al. 2016) in all seasons, with a secondary contribution from warming in the tropical Atlantic during austral winter and spring (Li et al. 2014; Simpkins et al. 2014). The observed cooling of the eastern tropical Pacific, associated with the transition of the Interdecadal Pacific Oscillation (IPO) to its negative phase after 1999 (Meehl et al. 2016) has also contributed to the slowdown in the rate of global warming (Trenberth and Fasullo 2013; Trenberth et al. 2014) as well as the strengthening of the Southern Hemisphere (SH) mid-latitude jet during summer and autumn (Clem et al. 2017b; Schneider et al. 2015).

Concurrent with the pressure decline over the ABS region, the surface pressure has been increasing across much of the subtropical Southern Oceans (30°-40°S), especially over the eastern half of the South Pacific (Fig. 1a), possibly in connection with an expansion of the Hadley cell (Garfinkel et al. 2015). A poleward shift of the cell's descending branch has been detected on a variety of observed metrics (Hu and Fu 2007; Lu et al. 2009) as well as in model simulations (Seidel et al. 2008; Hu et al. 2013). The Hadley cell expansion is also consistent with the strengthening / poleward shift of the mid-latitude westerly winds in the SH (e.g., Polvani et al. 2011) and a slight positive trend in the SAM (Previdi and Liepert 2007; Ablaster et al. 2011). The increasing anticyclonic circulation over the sub-tropical South Pacific directly influences eastern South Pacific SSTs by driving stronger equatorward, upwelling favorable winds along the west coast of South America resulting in a regional, off-equatorial surface cooling over the last several decades (Falvey and Garreaud 2009; Vuille et al. 2015). Moreover, the strengthening of this subtropical high-pressure cell has been associated with an intense multi-decadal drying trend over the subtropical southeast Pacific (Boisier et al. 2016) including a severe drought since 2010 in central Chile and the subtropical Andes (Garreaud et al. 2017; 2019) as well as western Argentina (Rivera et al. 2017).

The ridging at sub-tropical latitudes together with the negative SLP trends in the ABS region has resulted in a zonally elongated SLP trend dipole over the South Pacific (Fig. 1a) and associated strengthened mid-latitude westerlies over the South Pacific (Schneider et al. 2015). A similar dipolar structure was identified by You and Furtado (2017) as the leading mode of the SLP variability (termed as the South Pacific Oscillation; SPO). In the present study, we investigate the origin and climate impacts of the pressure trend dipole across the South Pacific during the last four decades, focusing on the extended SH winter season (May-September) when both the magnitude of the dipole trend and drying in western South America are strongest. Of relevance is assessing the role of natural modes of climate variability and anthropogenic forcing in sustaining the pressure trend dipole, a relevant task in the context of the ongoing climate change.

Several observational datasets (described in section 2a) are used to detect multi-decadal trends in the SH (section 3a) and determine the portion of them that are linearly congruent with sustained changes in tropical and high latitude climate modes (section 3b). To investigate the role of the SST changes (section 3c) upon tropospheric circulation and precipitation trends over the South Pacific we performed several numerical experiments using two Atmospheric GCMs of different level of complexity: CESM (Community Earth System Model) and SPEEDY (Simplified Parameterizations, primitivE-Equation DYnamics). The atmospheric simulations inform us on the direct atmospheric response to SST cooling or warming in specific areas of the tropical and subtropical oceans; however, it is important to note that they do not capture potential atmosphere-ocean feedbacks. With the CESM we conducted sensitivity experiments by adding a step function change to SST (section 2b) while SPEEDY was integrated in an AMIP style (sections 2c). Despite different modelling strategies, results from both sets of sensitivity experiments (sections 4a,b) suggest that a strong SST warming in the subtropical southwest Pacific (SSWP; Volstok et al 2017; Saurral el at. 2018) in recent decades plays a crucial role in producing the intensity and spatial extent of the South Pacific pressure trend dipole. The so-called Southern Blob seems to emerge in response to a significant reduction in convection in the central equatorial Pacific over the past four decades but it has continued unabated to present despite the negative phase of the IPO weakening after 2014 (Meehl et al. 2016). We also compare our observational and AGCM results to fully-coupled pre-industrial climate simulations from CMIP5 (section 4c) which capture both the large-scale processes tied to the emergence of the Southern Blob as well as its role in generating the South Pacific pressure trend dipole (section 5). A summary of our findings is presented in section 6.

2. Data and models

a. Observational datasets

The observational analyses generally span the last four decades (1979-2018), though a few datasets began their record in 1980 or 1981. We focus on the period May to September (MJJAS), the extended austral winter, because the pressure trend dipole is strongest over this period (see section 3a), it coincides with the rainy season in central Chile and subtropical Andes during which the ongoing drought in this region is at its peak (Garreaud et al. 2017), and tropical teleconnections in the SH are strongest over this period. Trends were calculated by linearly regressing (least-square mean method) a given variable over time. Statistical significance was assessed using a two-tailed Student's t-test on the regression slope (Wilks 1995).

The large-scale circulation was investigated using the European Centre for Medium-Range Weather Forecasts ERA5 Reanalysis (Hersbach et al. 2019), available from 1950 to present, including gridded (1.5°×1.5° lat-lon) monthly means of SLP and precipitation as well as geopotential height and air temperature at various pressure levels. Key results using ERA5 were compared to and are consistent with the National Center for Environmental Prediction – National Center for Atmospheric Research Renalysis (NNR, Kalnay et al. 1996), though these results should be taken with caution due to known spurious negative trends in pressure over the SH (Marshall 2013). Our study also employs monthly mean SST fields from the Hadley Centre Sea Ice and Sea Surface Temperature data set (HadISST 1.1) available from 1870 onwards on a 1°×1° lat-lon grid (Rayner et al. 2003), the NOAA Optimum Interpolation (OISST - V2) available from 1981 onwards on a 1°×1° lat-lon grid (Reynolds et al., 2002), and the NOAA Extended Reconstructed Sea Surface Temperature V5 (ERSSTv5) available from 1854 onwards on a 2°×2° lat-lon grid (Huang et al. 2017). The ocean warming was further studied using the NCEP Global Ocean Data Assimilation System (GODAS), a real-time ocean analysis with 40 vertical levels and 1° horizontal resolution (Behringer and Xue 2004) with monthly mean values since 1980. ERA5 precipitation trends were corroborated with monthly means of the NOAA Interpolated Outgoing Longwave Radiation (OLR) after 1979 on a 2.5°×2.5° lat-lon grid (Liebmann and. Smith 1996) as well as CPC Merged Analysis of Precipitation (CMAP) monthly dataset from 1979 that combines observations and satellite precipitation data into 2.5°×2.5° global grids (Xie and Arkin 1997).

b. CESM atmospheric only simulations

In section 4 we performed three sensitivity experiments using CESM version 1.2 (Hurrell et al. 2013) to determine the role of SST changes on the circulation trends and to isolate the direct effect of the SSWP warming (Table 1). The CESM was run in atmosphere-only mode using CAM5 physics and dynamics with prescribed SST and sea ice conditions (Hurrell et al. 2008), a horizontal resolution of 1.9°×2.5° lat-lon, and 30 vertical levels. Greenhouse gases (GHG) and stratospheric ozone (O3) concentrations were set at pre-industrial levels representative of the 1850s. We performed a total of three 30-year simulations each following a one-year spin up: (i) a control run with 1950-2017 monthly SST climatologies and default 1982-2001 monthly sea ice climatologies (CLIM), (ii) a full global SST trend run in which the

1979-2018 monthly SST trends (total change in the 40-year period) were added to the respective control monthly SST climatologies (CLIM+dSST), and (iii) as in (ii) but without the observed 1979-2018 SSWP warming (CLIM+dSST No SSWP) by applying a -1.5°C anomaly over the region 162.5-152.5°W, 33-40°S which removes the observed +1.5°C/40-yr warming observed there over 1979-2018 (see section 3c). The climatology and perturbed SST fields used in each experiment are shown in Sup. Fig. 1. We examine differences between simulated 30-year climatologies of SLP, 500 hPa geopotential height (Z500), precipitation and other fields of each run. These sensitivity simulations allow us to examine the role of the global ocean (full global SST trend) in causing the atmospheric circulation trends between 1979 and 2018 and the relative role of the SSWP SST warming within the global SST trend.

An additional sensitivity experiment performed with CESM was conducted to investigate the relative role of the observed decrease in precipitation over the central tropical Pacific (CPac) during 1979-2018. In this case we apply a negative SST anomaly (-1.5°C) over the region of observed reduced rainfall/positive OLR (centered at 180°, 6°S) which reproduces the local drying observed there. In all sensitivity experiments, the SST anomaly in the center of the target region diminishes to zero following a sine function over a 10° lat/lon at all sides of the anomaly box to avoid spurious SST gradients.

c. SPEEDY experiments

To corroborate the results from CESM, we used large ensembles of numerical experiments with SPEEDY (Kucharski et al. 2013). SPEEDY is an atmospheric global circulation model (AGCM) that solves the primitive equations with a spectral dynamical core and simplified physical parameterizations (large-scale condensation, shortwave and longwave radiation, shallow and deep convection, surface fluxes of momentum and energy, and vertical diffusion). The model resolution used is T30L8, which corresponds to a triangular spectral truncation with 30 wave numbers (96×48 Gaussian grid points), about 3.75°×3.75°, and eight vertical levels (Molteni 2003). Our SPEEDY simulations (Table 1) encompass the period 1960 - 2016 but trends were subsequently calculated using the model outputs over the last 40 years of the integration (1977-2016) that most closely match the observational period (1979-2018). (We also verified that observed circulation trends using 1977-2016 does not differ significantly from those using 1979-2018).

In contrast to CESM, the SPEEDY was integrated in an AMIP-like fashion in which we prescribed monthly varying ocean boundary conditions. In the control simulation the model was forced by the observed monthly SST and Sea Ice Concentration (SIC; Rayner et al. 2003) over the global oceans. In the sensitivity simulation the model was also forced by the observed SST and SIC except over the SSWP region where we keep repeating the mean climatological annual cycle (thus suppressing the SSWP warming). In both control and sensitivity experiments a total of 50 ensemble members were created by adding random diabatic forcing. Ensemble member 1 was perturbed 1 day (72-time steps), ensemble member 2 was perturbed for 2 days, and so on.

d. Fully coupled GCM simulations

Lastly, we used 51 fully coupled (ocean-atmosphere) pre-industrial control run simulations from the Coupled Model Intercomparison Project phase 5 (CMIP5) (Taylor et al., 2012). The models -identified in Sup. Table 1- have variable resolutions and were integrated for several hundred years under prescribed GHG and stratospheric O3 concentrations that are representative of pre-industrial conditions. These simulations reflect natural, unforced variability in the climate system.

3. Observed trends

a. The pressure trend dipole and the South Pacific drying band

Figure 1a shows the SLP trend during May - September (MJJS) from 1979 to 2018. Positive pressure trends dominate over the subtropical/midlatitude SH oceans (25°-45°S), with the largest values (>0.6 hPa/dec significant at $p<0.10$) across the South Pacific from the dateline to the west coast of South America. Positive trends are also significant over most of the South Atlantic. To the south of 45°S the trend pattern loses its zonal symmetry and is only significant over the ABS region where SLP has declined more than 1.0 hPa/dec during MJJS. The dipole in pressure trend is reminiscent of the South Pacific Oscillation identified by You and Furtado (2017) as the leading mode of interannual variability in this basin. Although our focus is on the winter, Sup. Fig. 2 also shows the SLP trends during summer. The summer trends are more zonally consistent and project strongly onto the SAM pattern, although the South Pacific pressure trend dipole is weaker.

To quantify the strength of the pressure trend dipole, we calculate the difference in SLP trend between the subtropical Pacific (40°-30°S; 210°-260°E) and the ABS region (70°-60°S; 230-280°E). The dipole is stronger from autumn to spring (Sup. Fig. 3), since the positive trends in the subtropical Pacific and the negative trends in the ABS are larger and consistent in the winter semester. Our results are in contrast to those of Turner et al. (2013) who found stronger negative trends in summer for the period 1979-2008, indicating the ABS pressure has recently begun deepening during winter after 2008 (Sup. Fig. 5). Furthermore, Turner et al. (2013) focuses on the deepening of the ASL (whose center moves through the year) while our trend calculation consider the broad and fixed ABS region.

The four-decade trend in Z500 during MJJAS (Fig. 1b) is consistent with the SLP trend, with a marked decrease over the ABS and ridging over the subtropical/midlatitude Pacific, thus revealing the quasi-barotropic nature of the pressure trend dipole. Geopotential height is strongly associated with mean temperature of the tropospheric column whereby warming of the column increases heights. Indeed, ERA5 data shows a warming trend throughout the troposphere across the Pacific between 30°-40°S (Sup. Fig. 4), which we later show is linked to the adjacent warming of sea surface temperatures.

Although the intensity of the pressure decline over the ABS region and subtropical Pacific ridging differs among datasets (Table 2) all of them reveal a significant South Pacific pressure trend dipole during the last four decades. The differences are most marked in the Antarctic periphery where the paucity of observations introduces larger uncertainties. The NNR SLP trend in the ABS is nearly twice larger than its ERA5 counterpart, which could be related to spurious trends in the former reanalysis (Marshall 2013). Nonetheless, the spatial pattern of the SLP trends is similar between both datasets (Sup. Fig. 2). Previous studies, which often consider a period ending before 2015, also found the subtropical Pacific ridging and the ABS low deepening (e.g., Trenberth et al. 2014). Indeed, using all possible combinations of initial and final years (if the period length is ≥10 years) we found that the SLP over the ABS (subtropical South Pacific) has been decreasing (increasing) until present (Sup. Fig. 5) meaning it is not fully explained by the negative IPO trend, which weakened after 2014, and also explains why our results differ from Turner et al. (2013) which did not find a deepened ASL in winter for their period ending in 2008; until that year the 40-year trends were positive over the ABS (Sup. Fig. 5a).

Collocated with the ridging across the South Pacific is an area of drying extending from about 30°S, 140°W to the west coast of South America (Fig. 1d). The four-decade precipitation decline over the eastern South Pacific based on ERA5 data is around -0.3 mm/day per decade and is statistically significant (p<0.10) in several portions of the ocean and along the Chilean coast. The drying suggested by the reanalysis data is confirmed with CMAP data and corroborated by positive OLR trends across the subtropical Pacific (Sup. Fig. 6). Moreover, over South America, *in-situ* records reveal a strong drying trend over the last 40 years in central-southern Chile, the subtropical Andes and parts of western Argentina (Boisier et al. 2016; 2019; Rivera et al. 2017). The drying has intensified since 2010 resulting in the so-called Central Chile mega drought with severe environmental and social impacts (Garreaud et al. 2017). Precipitation in this region is largely produced by extratropical frontal systems (Matthews 2012; Catto et al. 2012) and closely tied to the strength of the low- and mid-level westerlies (Garreaud 2007). Thus, precipitation decline is most likely due to weakened westerly winds and increased subsidence across the northern edge of the sub-tropical ridge. Meanwhile, the precipitation increases along the southern tip of the South America (Fig. 1d) is collocated with the region where westerlies have strengthened on the southern edge of the ridge. This subtropical – midlatitude contrast of precipitation trends over the southeast Pacific resembles the precipitation anomalies caused by the positive SAM phase (e.g., Fogt and Marshall 2020), but the SAM trend in winter is weak and insignificant pointing to other mechanism at play.

b. CPac-drying and SAM-congruent trend analysis

As mentioned previously, the observed pressure decrease over the ABS region (Fig. 1a; England et al. 2016; Raphael et al. 2016) has been attributed to teleconnections from the tropics (e.g., Ding and Steig 2013; Clem and Fogt 2015; Meehl et al. 2016), changes in the SAM (Turner et al. 2013), or a combination of both (Fogt and Bromwich 2006; Ding et al. 2012). We revisit these possible drivers by calculating the MJJAS SLP trends (1979-2018) that are linearly congruent (referred to as congruent trend; e.g. Thompson et al. 2000) with the observed trends in rainfall over the central tropical Pacific (CPac) and the positive trend in the Marshall (2003) SAM index. For a variable X at a given grid point, the SAM-congruent trend is estimated as $\beta\times\ \delta[SAM]$, where $\delta[SAM]$ is the linear trend of the SAM index (1979-2018) and β is the regression slope computed between SAM and X. The same procedure is done using positive trend in OLR averaged over the CPac region. Table 3 shows the correlation among the key indices in the period 1979-2018 using the original time series and their detrended versions. The congruency analysis highlights potentially important forcing mechanisms, which we later test with numerical experiments in section 4.

The CPac index (Fig. 2) is defined as the OLR averaged over the southern equatorial Pacific (170°E-168°W, eq-15°S) and exhibits a significant ($p<0.10$) positive trend (i.e., drying) during 1979-2018 (Fig. 2 and Sup. Fig. 6b). The SLP trend that is congruent with the CPac drying (Fig. 3a) is a PSA-like wave train resulting from the Rossby wave source in the exit region of the sub-tropical jet in the central South Pacific during winter (Lachlan-Cope and Connolley 2006; Yiu and Maycock 2019). This pattern strongly projects onto the observed (total) SLP trend: reduced convection in the central equatorial Pacific reduce pressure over the ABS region (including the ASL; Purich et al. 2016; Meehl et al. 2016) and increases pressure over parts of the subtropical Pacific. However, the CPac-drying congruent pressure trends are much weaker than the observed pressure trends, and moreover, they do not capture the eastern extension of the positive pressure trends over the eastern subtropical South Pacific close to the coast of South America (Fig. 3a).

The SAM index (Fig. 2) during MJJAS has a weak positive trend over 1979-2018 (insignificant at $p<0.10$), presumably tied to increased GHG and associated warming of the troposphere in lower latitudes (Cai and Cowan, 2006; Arblaster et al. 2011; Fogt and Marshall 2020). As expected, the SAM congruent SLP trends (Fig. 3b) are negative over Antarctica, encompassing much of the ABS region, and mostly positive at midlatitudes, except over the southeast Pacific where the SAM-related circulation anomalies are minimal due to the zonal wave three structure of the winter SAM pattern with mid-latitude circulation anomaly centers in the Indian Ocean, southwest Pacific, and South Atlantic (van Loon and Jenne 1972; Ding et al. 2012). Thus, the weak SAM trend seems to have a lesser contribution to the South Pacific pressure dipole than CPac drying, and moreover, it also does not project onto the eastward extent of the subtropical ridge toward South America.

The residual SLP trends (the portion of the observed trends not explained by the combined CPac drying plus positive SAM trend) are presented in Fig. 3c. The total SLP trend from CPac and SAM bears strong resemblance to the observed SLP trend across much of the SH but, importantly, capture only half the amplitude. Around 40% of the observed SLP decline over the ABS *is not* explained by combined CPac drying and positive SAM trend. Even more striking, more than 80% of the observed SLP increase over the subtropical southeast Pacific is not explained. Note that the interannual correlation between CPac OLR and the SAM indices (1979-2018, MJJAS) is very weak, only -0.1, (Table 3; see also L'Heureux and Thompson 2006). Therefore, the two trends and their linear congruent trends are largely independent; if anything, the weak correlation between the two would slightly overestimate the congruent portion of the observed circulation trends, and therefore the 40-80% of the circulation trends not explained by CPac and SAM is a conservative estimate. We also calculated the CPac/SAM congruent trends for Z500 and find similar results due to the equivalent barotropic structure of the extratropical SH circulation (Sup. Fig. 7). In sum, both the reduced rainfall over the central tropical Pacific and the weak positive SAM trend are relevant drivers of the multi-decadal pressure trend dipole over the South Pacific, but together they only explain about half of its intensity and even less of its eastward extent, indicating other mechanisms at play.

c. SST trends and the Southern Blob

Given its potential impact on the pressure trend dipole, we now examine SST trends over the last four decades. As before, we focus our analysis on MJJAS. Since the late 1970s, SST warming has dominated most of the world's oceans (~0.13°C/dec in average) but a few regions have experienced a cooling trend including the Southern Ocean and the eastern sub-tropical South Pacific (Fig. 1c). The largest warming in the whole Pacific basin (almost 0.4°C/dec, significant at $p<0.01$) is found over the subtropical southwest Pacific (SSWP, centered at 35°S, 160°W). The SST warming of the SSWP over the last four decades is seen across multiple datasets (Table 4) and is observed year-round but is strongest in winter (Sup. Fig. 3). From here on we refer to this warming as the *Southern Blob* given its impressive size and intensity. The rate of warming during winter has remained persistent throughout the past four decades (Saurral et al. 2018) indicative that the Southern Blob has emerged gradually and warmed continuously. Estimates of the ocean heat content (0-700 m) in this region reveal an increase over the last four decades, especially after 2010 (Fig. 4a). This result agrees with the satellite-based findings from Volkov et al. (2017) that report a significant deep-ocean warming in the SSWP accounting for up to a quarter of the global ocean heat increase in the period 2005-2014.

The vertical structure of the Southern Blob is shown by the time-depth Hovmöller diagram of the ocean potential temperature anomalies within the SSWP (Fig. 4b). The largest anomalies (~+0.5°C) have occurred in the upper 200 m, encompassing the mixed layer and the thermocline. There are also strong anomalies below 300 m in the early 1980s and late 2000s that seems unrelated to the Blob. The origin of the Southern Blob is discussed later in section 5.

4. Modeling results

a. Full SST simulations

We now investigate results from our sensitivity experiments with CESM and SPEEDY to better understand the relative roles of various SST changes in driving the MJJAS pressure trends over the South Pacific. Two CESM sensitivity experiments were performed to investigate the influence of 1979-2018 global SST trends thereby capturing potential contributions from all ocean basins. As described in section 2b, the experiments consist in a 30-year integration using a monthly climatology of SST (CLIM) and the climatology plus a monthly step function that represent the total change between 1979-2018 (CLIM+dSST). Table 1 summarizes the experiments and Sup. Fig. 1 shows the prescribed SST fields. The significance of the differences between CLIM+dSST and CLIM for selected variables was assessed using a two-tailed *t*-test.

The SLP/Z500 response to the 1979-2018 global SST trend (Fig. 5a,d) is in good agreement with the observed SLP/Z500 trends across the SH, including the pressure decrease over the ABS region (significant at $p<0.10$) and pressure increase over the subtropical South Pacific. The simulated intensity of the trend dipole (inferred from the total change in the 40-year period) is 60-70% of the observed intensity in ERA5. The CESM simulated precipitation differences between CLIM+dSST and CLIM (Fig. 5g) also aligns with the observed precipitation trends (Fig. 1d), with drying over the central equatorial Pacific and along a northwest-to-southeast diagonal band across the subtropical Pacific reaching the west coast of South America and increased precipitation south of the subtropical ridge, both significant at $p<0.10$.

In the case of SPEEDY (section 2c, Table 1), which we use to independently corroborate the CESM results, the control ensemble mean SLP trends (1977-2016 in this case) also exhibit a prominent dipole over the South Pacific (Figs. 6a), with a slightly weaker intensity compared with ERA5 but significant at $p<0.15$ using a Monte Carlo experiment (Sup. Fig. 8). Trends for each of the 50 members distribute over a wide range, but they are mostly positive over the subtropical Pacific and negative over the ABS region (Sup. Fig. 8). SPEEDY also reproduce a dipole in the trend of Z500 although displaced to the west of the observed pattern (Fig. 6d). The drying band extending across the subtropical south Pacific and reaching central Chile is also captured in the full AMIP ensemble mean using SPEEDY (Fig. 6g).

The overall agreement across the South Pacific between observed trends (Fig. 1) and their simulated counterparts using CESM and SPEEDY (Figs. 5 and 6, upper rows) forced with realistic SSTs implies that most of the pressure and precipitation trends over the South Pacific are, at first order, driven by concurrent SST changes in the global oceans. An obvious candidate is the central equatorial Pacific where SST and associated convective anomalies alter the extratropical circulation during winter by exciting the PSA pattern (Mo and Higgins 1998; Fig. 3a). Nevertheless, our regression analysis revealed that the observed CPac-related pressure trends explain less than half of the observed pressure decline over the ABS region and positive pressure trends are mostly absent over the eastern subtropical Pacific (section 3b).

b. SSWP warming sensitivity experiments

The direct impact of the Southern Blob on the pressure trends over the South Pacific is now investigated using numerical experiments designed to isolate the role of SSWP warming. In CESM we conducted an additional 30-year integration identical to CLIM+dSST but removing the SSWP warming (see Section 2 and Table 1) and replacing with the climatological seasonal cycle of the control run. Note that the area affected by this substitution represent less than 1% of the global ocean. The global SST trend without SSWP warming experiment informs us of the trends in the atmospheric circulation that would have emerged from the global change in SST but *without* the influence of the Southern Blob. Figure 5b shows this altered SLP trend, which mostly retains the CPac-PSA pattern, but the South Pacific dipole is weakened by about half. Similar results are found in Z500 (Fig. 5e). The SST-forced precipitation trend still features the drying over the CPac region, implying that this feature is caused by SST trends not related to SSWP warming (e.g., they likely emerge from the tropical Pacific SST trends), but the dry diagonal band extending to central Chile conspicuously disappeared after removing SSWP warming (Fig. 5h).

The difference between the atmospheric trends simulated by CESM with and without SSWP warming provides an estimate of the Southern Blob direct effects (recall that our atmosphere-only simulations reveal the *direct* effect of the SST but do not capture atmosphere-ocean feedbacks). The maps in the bottom row in Fig. 5 shows that SSWP warming forces a SLP decline of around -2 hPa (-0.5 hPa/dec) on the western side of the ABS region (significant at $p<0.10$ over the Ross sea) and a strong SLP increase of around +1.6 hPa (+0.4 hPa/dec) across the South Pacific centered at 35°-40°S (significant at $p<0.10$ from 120°W to the Chilean coast). Notably, the direct impact of the Southern Blob in the pressure trend are quite similar to the residual not explained by CPac drying plus positive SAM trend in our congruency analysis (Fig. 3c) with the only exception being that the strongest blob-related ABS deepening is to the west of the area where the residual is largest. Furthermore, nearly all the sub-tropical South Pacific pressure increases east of 150°W are tied to the SSWP warming. Likewise, the Southern Blob explains most of the drying between 30-40°S in the far eastern South Pacific near the coast of central South America (Fig. 5i) confirming previous claims on its key role in driving the central Chile mega drought (Garreaud et al. 2019).

Again, to test the results in CESM, a second 50-member ensemble run was carried out with SPEEDY forced by the observed SST except over the SSWP region where SST is kept to the mean climatological annual cycle (Table 1). The ensemble mean pressure trends in the no-SSWP simulation still exhibit ridging over the subtropical Pacific and deepening over the west flank of the ABS region but they are about half of the trends in the control (full SST) simulations (middle row in Fig. 6 and Sup. Fig. 8). To depict the Southern Blob direct effect as per SPEEDY simulations, the bottom panels in Fig. 6 show the difference between SLP, Z500 and precipitation trends with and without the SSWP warming. The warming of the SSWP emerges as the dominant driver of the positive pressure trends (Figs. 6c,f) and drying (Fig. 6i) in the far east subtropical Pacific, central Chile and the subtropical Andes, and also contributes to the pressure decrease over the western half of the ABS region.

Therefore, two GCMs -with different levels of complexity- show that the strong warming of the SSWP accounts for about half of the pressure decline over the western half of ABS region and nearly all of the ridging over the far eastern subtropical South Pacific, thus accounting for much of the residual of CPac drying and positive SAM. The Southern Blob thus emerges as a key element in the pressure trend dipole over the South Pacific during the last four decades, acting in concert with long-term changes in connection with CPac drying and positive SAM trends.

c. Fully coupled model results

Next, we examine the dynamical response to the Southern Blob across a much larger range of possible background conditions using the ensemble of 51 CMIP5 pre-industrial control runs (section 2). As these simulations are fully coupled, this analysis also captures feedbacks between atmosphere and ocean. First, we calculated all possible 40-year SST trends in the SSWP for each ensemble member and retain only the 40-year interval over which the largest trend occurred in each ensemble member. Figure 7 shows the multi-model mean SST, SLP, and precipitation trend for the strongest 40-year warming periods. The Southern Blob, as simulated in these coupled models, is associated with a South Pacific pressure trend dipole similar to the observed pressure trend over 1979-2018, including the elongated ridge extending across the midlatitude Pacific from New Zealand to the coast of Chile and the pressure decline over the ABS region, as well as a reduction in rainfall in the southeast Pacific and central Chile between 30-40°S. Also relevant is that the large-scale pattern accompanying strong SSWP warming consists of reduced rainfall in CPac and a positive SAM pattern (Fig. 7), which suggests these climate patterns are relevant features of strong SSWP warming, likely in the development and maintenance of the Southern Blob.

Now we compare the observed warming rate of the Southern Blob to the highest 40-year SSWP warming rates simulated in the pre-industrial models (Fig. 8). The recent warming (+1.4°C/40-yr) exceeds all possible simulated 40-year warming trends that arise from natural (unforced) variability in the CMIP5 pre-industrial models. Assuming that the model variability in this large ensemble of pre-industrial simulations is representative of the internal climate variability we can infer that the current magnitude of SSWP warming likely would not arise under natural multi-decadal climate variability alone, and it appears that external forcing, such as radiative forcing from increasing GHG concentrations, has likely contributed to the remarkable rate of warming in this region of the Pacific over the past 40 years. The SST response to current anthropogenic forcing has been estimated from the multi-model mean trend in the merged historical and RCP8.5 (post 2006) simulations that contain observed, time-varying external forcing such as recent anthropogenic increases in GHG concentrations (e.g., Cubash et al. 2001; Funk and Hoell 2015). While in the equatorial region the strongest warming is over the eastern Pacific the pattern reverses in the extratropical South Pacific, with the anthropogenic warming being stronger in the west. These results support the notion that a long-lived Southern Blob can emerge naturally in the SSWP associated with CPac drying and positive SAM, but its exceptional intensity over the past 40 years–along with the dynamical response– has been aided by anthropogenic forcing.

5. Discussion

In the previous section we have documented the pressure trend dipole between the subtropical Pacific and the Antarctic periphery using observational datasets. Sensitivity experiments using atmospheric simulations further suggest that part of these trends appear in connection with the marked surface warming over the SSWP. In this section we advance some hypothesis on the origin of the blob and how it can force such atmospheric responses.

The linear congruency results along with the spatial trend pattern from CESM and SPEEDY experiments without SSWP warming suggest that anomalous reductions in precipitation over CPac would produce, by itself, anomalous ridging east of New Zealand and a pressure decline over the ABS region tied to its generation of the PSA pattern. This is consistent with previous findings (e.g., Trenberth et al. 2014; Meehl et al. 2016) and further confirmed by our own CPac sensitivity experiment we performed with CESM in which we applied a negative SST anomaly in the region of observed reduced rainfall/positive OLR (180°, 6°S) (Fig. 9). Indeed, Z500 and 250 hPa streamfunction anomalies reveal the PSA-like response to this perturbation with ridging in the subtropical Pacific and deepening near the Antarctic periphery. The PSA-related ridging at subtropical latitudes, however, does not reach the west coast of South America. Notably, an anomalous Rossby wave source is established along the sub-tropical jet at 30°S between 180-150°W, resulting in an anticyclone over and just east of the Southern Blob.

We speculate that anomalous easterly/northeasterly surface winds on the northern and western edge of the PSA ridge transports warm sub-tropical water into the Southern Blob and favors anomalous downwelling due to anticyclonic wind stress curl to the left (on the poleward side) of the easterlies. The subsidence associated with the ridge would also favor calm winds (reduced ocean mixing) and reduced cloud cover immediately over the Blob increasing the oceanic absorption of incoming shortwave radiation and warming the surface. Therefore, we posit that the development of the Southern Blob during 1979-2018 is dynamically tied to the observed drying in CPac and the associated PSA pattern (Fig. 10a). Indeed, the winter CPac-OLR and SSWP SST are highly correlated (Table 3).

We note, however, that more than 70% of the winter SST trend from 1979 to 2018 over the SSWP *is not explained* by the CPac drying, and therefore positive atmosphere-ocean feedbacks between the SSWP warming and associated ridging are likely at play. Exploring such feedbacks will require fully coupled simulations and/or OMIP (ocean only) simulations and should be the subject of future work. Likewise, the exceptional warming rate and heat content over the past 40 years in the SSWP suggest the influence of anthropogenic forcing and calls for further studies.

The accumulation of heat in the upper ocean of the Southern Blob would then be transferred to the atmospheric boundary layer and eventually to the whole tropospheric column (Sup. Fig. 4). The mid-level warming and ridging extend well beyond the SSWP region, reaching the far eastern South Pacific. Indeed, 1979-2018 trends in ERA5 thermal advection (Sup. Fig. 9) show a significant increase in eastward warm air advection toward South America sourced over the SSWP warming region. This would increase geopotential heights and result in downstream ridge building over the eastern sub-tropical South Pacific (Fig. 10b).

Our numerical experiments also suggest the SSWP warming contributes to the recent MJJAS pressure decline over the ABS region (Figs. 5c and 6c), specially between 180-120°W (Fig. 10b). To investigate the mechanisms at play, we examine the trends in ERA5 of the **Eu** vector. This vector is the horizontal, local expression of the Eliassen-Palm (E-P) Flux useful for gauging the effect of the Eddies on the zonal mean flow (Trenberth 1991). South of the anomalous ridge associated with SSWP warming (190-210E) there is increased poleward momentum flux and momentum flux convergence over the western flank of the ABS region (Sup. Fig. 10). This results in strong westerly wind production in the mid-latitude jet which is associated with a regional poleward shift of the mid-latitude jet/storm track (e.g. Barnes and Polvani 2013). Therefore, the SSWP warming may partially force the weak positive SAM trend (e.g., Ding et al. 2012) through a combination of strengthening north-south temperature gradient over the mid to high latitude South Pacific (via thermal wind balance) in addition to strengthening poleward momentum fluxes and momentum flux convergence.

6. Concluding remarks

In this study we have examined the dipolar structure that characterizes the pressure trend across the South Pacific in the last four decades. We documented its connection to precipitation and examined its dynamical origin by using regression analysis and atmospheric numerical experiments from two AGCMs (CESM and SPEEDY). Our main findings and results are presented below:

- The pressure trends from 1979 to 2018 feature an equivalent barotropic, north-south dipole over the South Pacific, with ridging at subtropical latitudes (most marked in the eastern South Pacific) and pressure decline over the ABS region. The trends are significant and strongest in austral winter (May-September). Previous studies have linked these trends with sea surface cooling off the west coast of South America (Falvey and Garreaud 2009; Vuille et al. 2015), severe drought in central Chile (Garreaud et al. 2019), as well as sea ice expansion in the Ross Sea and sea ice loss/surface warming along the Antarctic Peninsula (e.g., Purich et al. 2016; Meehl et al. 2016).

- The sea surface cooling and reduced rainfall over the central and eastern tropical Pacific (e.g., Meehl et al. 2016) and the weak positive trend in the SAM index during winter (e.g., Fogt and Marshall 2020) are relevant drivers of the multi-decadal pressure trend dipole. Our linear congruency analysis, however, indicates that their combined effect explains only about half of the observed intensity of the pressure trend dipole during 1979-2018.

- Two sets of atmospheric model experiments (adding a step function SST change with CESM and time varying SST (AMIP style) with SPEEDY) suggest that most of the South Pacific pressure trend dipole and subtropical drying are caused by SST trends in the global oceans. A "region of interest" is the subtropical southwest Pacific that has experienced a strong warming since the early 1980s to date, and which we refer to as the Southern Blob. The sea surface warming is evident in multiple data sets and the Blob to extends down to ~200 m.

- Sensitivity experiments (no-SSWP warming) designed to isolate the effect of the SSWP reveal the contribution of the Southern Blob in producing the pressure trend dipole over the South Pacific during the last four decades.

This SSWP warming acts in tandem with the CPac drying and positive SAM trend to further reduce the pressure over the ABS region, especially in its the western portion where the Blob generates poleward momentum fluxes and locally enhances the the north-south temperature gradient. Further, the numerical experiments indicate that Blob accounts for nearly all of the eastward extension of the subtropical ridging and the drying over the far eastern South Pacific and the adjacent South American coast between 30°-40°S.

- Preindustrial, fully coupled simulations feature multi-decadal periods of SSWP warming that are also associated with CPac drying. This suggests that the Southern Blob –along with its remote impacts- can emerge naturally in association with the Pacific-South American pattern. The current rate of warming in the Southern Blob, however, exceeds the range of natural variability inferred by the pre-industrial inter model variability, suggesting an anthropogenic contribution to the current rate of SSWP warming. The precise mechanisms by which anthropogenic forcing augments the intensity of the Southern Blob –along with its remote impacts- requires further research.

In sum, our results show the Southern Blob has emerged gradually and warmed continuously over the past 40 years, is most marked during austral winter and remarkably accounts for up to a quarter of the global ocean heat increase in the period 2005-2014 (Volkov et al. 2017). Based on numerical experiments conducted with two AGCMs we found that the warming in the SSWP had had a profound influence over the South Pacific where it has caused significant pressure and geopotential height increases at subtropical latitudes extending to the coast of central Chile. This ridging has shifted the storm track poleward into the ABS region and away from central Chile, thereby contributing to around half of the observed pressure decline over the ABS region (most marked around 150°W) and nearly all the precipitation decline across central Chile where a severe "Megadrought" is ongoing. Examining pre-industrial climate model simulations we found that the Blob and associated teleconnections can emerge naturally, but the current rate of warming is exceptional, perhaps forced externally. By extension, these results may be useful in understanding other anthropogenically-forced drying regions projected by climate models in west coast Mediterranean climates in the Pacific, such as southwest North America and California.

Data Availability Statement. All dataset from public domains. Please refer to section 2 for further details.

Acknowledgments. We thank Roberto Rondanelli and Juan Pablo Boisier for constructive comments and suggestions on the original draft. SPEEDY simulations were performed and processes by H. Sepulveda and D. Veloso, Universidad de Concepción, Chile. CESM simulations were performed by KRC on the Rutgers University Amarel High Performance Community Cluster. The Center for Climate and Resilience Research (CR2, CONICYT / FONDAP / 15110009) provided partial funding for RG. KRC acknowledges postdoctoral support from Rutgers University and Victoria University of Wellington. We acknowledge the World Climate Research Programme's Working Group on Coupled Modelling, which is responsible for CMIP, and we thank the climate modeling groups (listed in Sup. Table 1 of this paper) for producing and making available their model output. For CMIP the U.S. Department of Energy's Program for Climate Model Diagnosis and Intercomparison provides coordinating support and led development of software infrastructure in partnership with the Global Organization for Earth System Science Portals. We acknowledge Copernicus Climate Change Service (C3S) and ECMWF for providing ERA-5 data; NOAA Physical Sciences Laboratory (PSL) for providing NCEP-NCAR Reanalysis, CMAP, OLR, OISST and GODAS data.

References

Allan, R., and T. Ansell, 2006: A New Globally Complete Monthly Historical Gridded Mean Sea Level Pressure Dataset (HadSLP2): 1850-2004. *J. Climate*, **19**, 5816-5842

Arblaster, J.M., G.A. Meehl and D.J. Karoly, 2011: Future climate change in the Southern Hemisphere: Competing effects of ozone and greenhouse gases. *Geophys. Res. Lett.*, **38**,L02701

Baines, P. G., and K. Fraedrich, 1989: Topographic Effects on the Mean Tropospheric Flow Patterns around Antarctica. *J. Atmospheric Sci.*, **46**, 3401–3415, https://doi.org/10.1175/1520-0469(1989)046<3401:TEOTMT>2.0.CO;2.

Behringer, D.W., and Y. Xue, 2004: Evaluation of the global ocean data assimilation system at NCEP: The Pacific Ocean. Eighth Symposium on Integrated Observing and Assimilation Systems for Atmosphere, Oceans, and Land Surface, AMS 84th Annual Meeting, Washington State Convention and Trade Center, Seattle, Washington, 11-15.

Boisier, J.P., R. Rondanelli, R. Garreaud, F. Muñoz, 2016: Natural and anthropogenic contributions to the Southeast Pacific precipitation decline and recent mega-drought in central Chile. *Geophys. Res. Lett.,* **43**, doi:10.1002/2015GL067265

Boisier, J.P., C. Alvarez-Garreton, R. Cordero, A. Damian, L. Gallardo, R. Garreaud, F. Lambert, C. Ramallo, M. Rojas and R. Rondanelli, 2019: Anthropogenic drying in central-southern Chile evidenced by long term observations and climate model simulations. *Elem Sci Anth,* **6**, 74. DOI: http://doi.org/10.1525/elementa.328

Bond, N.A., MF. Cronin, H. Freeland and N. Mantua, 2015: Causes and impacts of the 2014 warm anomaly in the NE Pacific. *Geophys. Res. Lett.*, **42**(9): 3414- 3420, doi: 10.1002/2015GL063306.

Bromwich, D. H., J. P. Nicolas, A. J. Monaghan, M. A. Lazzara, L. M. Keller, G. A. Weidner, and A. B. Wilson, 2012: Central West Antarctica among the most rapidly warming regions on Earth. *Nat. Geosci.*, **6**, 139–145, https://doi.org/10.1038/ngeo1671.

Cai, W. and T. Cowan, 2006: SAM and regional rainfall in IPCC AR4 models: Can anthropogenic forcing account for southwest Western Australian winter rainfall reduction? Geophysical Research Letters, **33**, L24708, doi:10.1029/2006GL028037

Catto, J., C. Jakob, G. Berry, and N. Nicholls, 2012: Relating global precipitation to atmospheric fronts. *Geophys. Res. Lett.*, **39**, L10805, doi:10.1029/2012GL051736

Cionni, I., V. Eyring, J, Lamarque, W. Randel, D. Stevenson, F. Wu, G. Bodeker, T. Shepherd, D. Shindell and D. and Waugh, 2011: Ozone database in support of CMIP5 simulations: results and corresponding radiative forcing. *Atmospheric Chemistry and Physics*, **11**, 11267–11292

Clem, K. R., and R. L. Fogt, 2015: South Pacific circulation changes and their connection to the tropics and regional Antarctic warming in austral spring, 1979-2012: S. Pacific Trends and Tropical Influence. *J. Geophys. Res. Atmospheres*, **120**, 2773–2792, https://doi.org/10.1002/2014JD022940.

——, J. A. Renwick, and J. McGregor, 2017a: Large-Scale Forcing of the Amundsen Sea Low and Its Influence on Sea Ice and West Antarctic Temperature. *J. Clim.*, **30**, 8405–8424, https://doi.org/10.1175/JCLI-D-16-0891.1.

——, ——, and ——, 2017b: Relationship between eastern tropical Pacific cooling and recent trends in the Southern Hemisphere zonal-mean circulation. *Clim. Dyn.*, **49**, 113–129, https://doi.org/10.1007/s00382-016-3329-7.

Connolley, W. M., 1997: Variability in annual mean circulation in southern high latitudes. *Clim. Dyn.*, **13**, 745–756.

Cubasch, U., and Coauthors, 2001: Projections of future climate change. Climate Change 2001: The Scientific Basis, J. T. Houghton et al., Eds., Cambridge University Press, 527–582

Dee, D., S. Uppala, A. Simmons, P. Berrisford, P. Poli, S. Kobayashi, U. Andrae, M. Balmaseda, G. Balsamo, and P. Bauer, 2011: The ERA-Interim reanalysis: configuration and performance of the data assimilation system, *QJ Roy. Meteor. Soc.*, **137**, 553–597.

Ding, Q., and E. J. Steig, 2013: Temperature change on the Antarctic Peninsula linked to the tropical Pacific. *J. Clim.*, **26**, 7570–7585.

——, ——, D. S. Battisti, and J. M. Wallace, 2012: Influence of the Tropics on the Southern Annular Mode. *J. Clim.*, **25**, 6330–6348, https://doi.org/10.1175/JCLI-D-11-00523.1.

Falvey, M. and R. Garreaud, 2009: Regional cooling in a warming world: Recent temperature trends in the SE Pacific and along the west coast of subtropical South America (1979-2006). *J. Geophys. Res.*, **114**, D04102, doi:10.1029/2008JD010519

Flatau, M., and Y.-J. Kim, 2013: Interaction between the MJO and Polar Circulations. *J. Clim.*, **26**, 3562–3574, https://doi.org/10.1175/JCLI-D-11-00508.1.

Fogt, R. L., and D. H. Bromwich, 2006: Decadal variability of the ENSO teleconnection to the high-latitude South Pacific governed by coupling with the southern annular mode. *J. Clim.*, **19**, 979–997.

——, A. J. Wovrosh, R. A. Langen, and I. Simmonds, 2012: The characteristic variability and connection to the underlying synoptic activity of the Amundsen-Bellingshausen Seas Low: THE AMUNDSEN-BELLINGSHAUSEN SEAS LOW. *J. Geophys. Res. Atmospheres*, **117**, n/a-n/a, https://doi.org/10.1029/2011JD017337.

Funk, C., and A. Hoell, 2015: The Leading Mode of Observed and CMIP5 ENSO Residual Sea Surface Temperatures and Associated Changes in Indo-Pacific Climate *J. Clim*., **28**, 4309–4329. https://doi.org/10.1175/JCLI-D-14-00334.1

Garfinkel, C. I., D. W. Waugh, and L. M. Polvani, 2015: Recent Hadley cell expansion: The role of internal atmospheric variability in reconciling modeled and observed trends: MODELS CAPTURE HC SHIFT. *Geophys. Res. Lett.*, **42**, 10,824-10,831, https://doi.org/10.1002/2015GL066942.

Garreaud, R. D., 2007: Precipitation and circulation covariability in the extratropics, *J. Clim.*, **20**, 4789-4797.

Garreaud, R., P. Lopez, M. Minvielle and M. Rojas, 2013: Large Scale Control on the Patagonia Climate. *J. of Climate*, **26**, 215-230

Garreaud, R.D., C. Alvarez-Garreton, J. Barichivich, J.P., Boisier, D. Christie, M. Galleguillos, C. LeQuesne, J. McPhee, M. Zambrano-Bigiarini, 2017: The 2010–2015 megadrought in cen¬tral Chile: Impacts on regional hydroclimate and vegetation. *Hydrol Earth Syst Sci*, **21**: 6307–6327. DOI: https://doi.org/10.5194/hess-21-6307-2017

Garreaud, R.D., J.P. Boisier, R. Rondanelli, A. Montecinos, H. Sepúlveda and D. Veloso-Águila, 2019: The Central Chile Mega Drought (2010-2018): A Climate dynamics perspective. *International Journal of Climatology*, **40**, 421-439 https://doi.org/10.1002/joc.6219

Gillett, N. P., T. D. Kell, and P. Jones, 2006: Regional climate impacts of the Southern Annular Mode. *Geophys. Res. Lett.*, **33**, L23704, doi:10.1029/2006GL027721

Henderson, S. A., and E. D. Maloney, 2018: The Impact of the Madden–Julian Oscillation on High-Latitude Winter Blocking during El Niño–Southern Oscillation Events. *J. Clim.*, **31**, 5293–5318, https://doi.org/10.1175/JCLI-D-17-0721.1.

Henley, B. J., J. Gergis, D. J. Karoly, S. Power, J. Kennedy, and C. K. Folland, 2015: A Tripole Index for the Interdecadal Pacific Oscillation. *Clim. Dyn.*, **45**, 3077–3090, https://doi.org/10.1007/s00382-015-2525-1.

Hersbach, H., and co-authros, 2018: Operational global reanalysis: Progress, future directions and synergies with NWP. European Centre for Medium Range Weather Forecasts. ERA Report Series No. 27. 63 pp.

Huang, B., and Coauthors, 2017: Extended Reconstructed Sea Surface Temperature, Version 5 (ERSSTv5): Upgrades, Validations, and Intercomparisons. *J. Clim.*, **30**, 8179–8205, https://doi.org/10.1175/JCLI-D-16-0836.1.

Hurrell, J. W., J. J. Hack, D. Shea, J. M. Caron, and J. Rosinski, 2008: A New Sea Surface Temperature and Sea Ice Boundary Dataset for the Community Atmosphere Model. *J. Clim.*, **21**, 5145–5153, https://doi.org/10.1175/2008JCLI2292.1.

——, and Coauthors, 2013: The Community Earth System Model: A Framework for Collaborative Research. *Bull. Am. Meteorol. Soc.*, **94**, 1339–1360, https://doi.org/10.1175/BAMS-D-12-00121.1.

Hu, Y. and Q. Fu, 2007: Observed poleward expansion of the Hadley circulation since 1979. *Atmos. Chem. Phys*., **7**, 5229–5236

Hu, Y., L. Tao and J. Liu, 2013: Poleward Expansion of the Hadley Circulation in CMIP5 Simulations. *Adv. in Atmos. Sciences*, **30**, 790-795.

Irving, D., and I. Simmonds, 2016: A New Method for Identifying the Pacific–South American Pattern and Its Influence on Regional Climate Variability. *J. Climate*, **29**, 6109–6125, https://doi.org/10.1175/JCLI-D-15-0843.1.

Jones, J., Gille, S., Goosse, H. et al., 2016: Assessing recent trends in high-latitude Southern Hemisphere surface climate. *Nature Clim Change* **6**, 917–926. https://doi.org/10.1038/nclimate3103

Kalnay, E., Kanamitsu, M., Kistler, R., Collins, W., Deaven, D., Gandin, L., Iredell, M., Saha, S., White, G. and Woollen, J., 1996: The NCEP/NCAR 40-year reanalysis project. Bulletin of the American Meteorological Society, 77, 437–471.

Kanamitsu, M., W. Ebisuzaki, J. Woollen, S-K Yang, J.J. Hnilo, M. Fiorino, and G. L. Potter, 2002: NCEP-DOE AMIP-II Reanalysis (R-2). *Bull. Am. Meteorol. Soc.,* **102***,* 1631-1643.

Kucharski, F., F. Molteni, M. King, R. Farneti, I. Kang, and L. Feudale, 2013: On the need of intermediate complexity general circulation models: a "SPEEDY" example. *Bull. Am. Meteorol. Soc.*, **94**, 25–30

Lachlan-Cope, T., Connolley, W. and Turner, J. 2001: The role of the non-axisymmetric antarctic orography in forcing the observed pattern of variability of the Antarctic climate. *Geophys. Res. Lett.,* **28**, https://doi.org/10.1029/2001GL013465

Lachlan-Cope, T., and W. Connolley, 2006: Teleconnections between the tropical Pacific and the Amundsen-Bellinghausens Sea: Role of the El Niño/Southern Oscillation: TROPICAL HIGH-LATITUDE TELECONNECTIONS. *J. Geophys. Res. Atmospheres*, **111**, n/a-n/a, https://doi.org/10.1029/2005JD006386.

Lee, H.-J., and K.-H. Seo, 2019: Impact of the Madden-Julian oscillation on Antarctic sea ice and its dynamical mechanism. *Sci. Rep.*, **9**, 10761, https://doi.org/10.1038/s41598-019-47150-3.

L'Heureux, M. L., and Coauthors, 2017: Observing and Predicting the 2015/16 El Niño. *Bull. Am. Meteorol. Soc.*, **98**, 1363–1382, https://doi.org/10.1175/BAMS-D-16-0009.1.

Li, X., D. M. Holland, E. P. Gerber, and C. Yoo, 2014: Impacts of the north and tropical Atlantic Ocean on the Antarctic Peninsula and sea ice. *Nature*, **505**, 538–542, https://doi.org/10.1038/nature1294|5.

Li, X., D. M. Holland, E. P. Gerber, and C. Yoo, 2015: Rossby Waves Mediate Impacts of Tropical Oceans on West Antarctic Atmospheric Circulation in Austral Winter. J. Climate, 28, 8151–8164, https://doi.org/10.1175/JCLI-D-15-0113.1.

Liebmann B. and C.A. Smith, 1996: Description of a Complete (Interpolated) Outgoing Longwave Radiation Dataset. *ull. Amer. Meteor. Soc.*, **77**, 1275-1277.

Lu, J., C. Deser and T. Reichler, 2009: Cause of the widening of the tropical belt since 1958. *Geophys. Res. Lett.,* **36**, L03803, doi:10.1029/2008GL036076, 2009

van Loon, H., and R. L. Jenne, 1972: The zonal harmonic standing waves in the southern hemisphere. *J. Geophys. Res.*, **77**, 992–1003, https://doi.org/10.1029/JC077i006p00992.

Marshall, G. J., 2003: Trends in the southern annular mode from observations and reanalyses. *J. Clim.*, **16**, 4134–4143, https://doi.org/10.1175/1520-0442(2003)016<4134:TITSAM>2.0.CO;2.

Matthews, A. J., 2012: A multiscale framework for the origin and variability of the South Pacific Convergence Zone. *Q. J. R. Meteorol. Soc.*, **138**, 1165–1178, https://doi.org/10.1002/qj.1870.

MacDonald G.M. and R.A. Case, 2005: Variations in the Pacific Decadal Oscillation over the past millennium. *Geophys. Res. Lett.* 32, L08703, doi:10.1029/2005GL022478.

Meehl, G. A., J. M. Arblaster, C. M. Bitz, C. T. Y. Chung, and H. Teng, 2016: Antarctic sea-ice expansion between 2000 and 2014 driven by tropical Pacific decadal climate variability. *Nat. Geosci.*, **advance online publication**, https://doi.org/10.1038/ngeo2751.

Mo, K. C., and R. W. Higgins, 1998: The Pacific–South American Modes and Tropical Convection during the Southern Hemisphere Winter. *Mon. Weather Rev.*, **126**, 1581–1596, https://doi.org/10.1175/1520-0493(1998)126<1581:TPSAMA>2.0.CO;2.

Molteni, F., 2003: Atmospheric simulations using a GCM with simplified physical parametrizations. I: model climatology and variability in multi-decadal experiments. Climate Dynamics, 20, 175–191

Montecinos, A., A. Díaz, and P. Aceituno, 2000: Seasonal Diagnostic and Predictability of Rainfall in Subtropical South America Based on Tropical Pacific SST. J. Climate, 13, 746–758, https://doi.org/10.1175/1520-0442(2000)013<0746:SDAPOR>2.0.CO;2.

Polvani, L.M., Waugh, D.W., Correa, G.J. and Son, S.W., 2011: Stratospheric ozone depletion: The main driver of twentieth-century atmospheric circulation changes in the Southern Hemisphere. Journal of Climate, 24(3), 795-812.

Previdi, M. and G.B. Liepert, 2007: Annular modes and Hadley cell expansion under global warming. *Geophys. Res. Lett.*, **34**, L22701, doi:10.1029/2007GL031243

Purich, A., M. England, W. Cai, Y. Chikamoto, A. Timmermann, J.C. Fyfe, L. Frankcombe, G.A. Meehl, and J. Arblaster, 2016: Tropical pacific SST drivers of recent antarctic sea ice trends. *J. Clim.,* **29**, 8931-8948

Raphael, M.N., G. J. Marshall, J. Turnrner, R. L. Fogtgt, D. Schneider, D. A. Dixon, J. S. Hoskingng, J. M. Jones, andnd W. R. Hobbs, 2016: The Amundsen Sea low: Variability, change, and impact on Antarctic climate. *Bull. Amer. Meteor. Soc.*, **97**, 111–121, doi:10.1175/BAMS-D-14-00018.1

Rayner, N. A., Parker, D. E., Horton, E. B., Folland, C. K., Alexander, L. V., Rowell, D. P., Kent, E. C. and Kaplan, A., 2003: Global analyses of sea surface temperature, sea ice, and night marine air temperature since the late nineteenth century *J. Geophys. Res.* **108**, No. D14, 4407 10.1029/2002JD002670

Reynolds, R. W., T. Smith, C. Liu, D.B. Chelton, K.S. Casey, M.G. Schlax, 2007: Daily High-Resolution-Blended Analyses for Sea Surface Temperature. *J. Clim.*, **20**, 5473-5496.

Rivera, J., O. Penalba, R. Villalba and D. Araneo, 2017: Spatiotemporal patterns of the 2010–2015 extreme hydrological drought across the Central Andes, Argentina. *Water*, **9**, 652-669.

Roxy, M.K., Dasgupta, P., McPhaden, M.J., Suematsu, T., Zhang, C. and Kim, D., 2019: Twofold expansion of the Indo-Pacific warm pool warps the MJO life cycle. *Nature*, **575**(7784), 647-651.

Saurral, R., F. Doblas-Reyes and J. García-Serrano, 2018: Observed modes of sea surface temperature variability in the South Pacific region. *Climate Dynamics*, **50**, 1129–1143

Schneider, D. P., C. Deser, and T. Fan, 2015: Comparing the Impacts of Tropical SST Variability and Polar Stratospheric Ozone Loss on the Southern Ocean Westerly Winds. *J. Clim.*, **28**, 9350–9372, https://doi.org/10.1175/JCLI-D-15-0090.1.

Seidel, D. J., Q. Fu, W. J. Randel, and T. J. Reichler, 2008: Widening of the tropical belt in a changing climate. *Nat. Geosci.*, **1**, 21–24, https://doi.org/10.1038/ngeo.2007.38.

Simpkins, G. R., S. McGregor,A. S. Taschetto, L. M. Ciasto, and M. H. England,2014: Tropical connections to climatic change in the extratropical Southern Hemisphere: The role of Atlantic SST trends. *J. Clim.*, **27**, 4923–4936, doi:10.1175/JCLI-D-13-00615.1.

Stammerjohn, S., Massom, R., Rind, D., and Martinson, D. (2012), Regions of rapid sea ice change: An inter-hemispheric seasonal comparison, *Geophys. Res. Lett.*, **39**, L06501, doi:10.1029/2012GL050874.

Taylor, K., R. Stouffer, G. Meehl, 2012: An overview of CMIP5 and the experiment design. *Bull. Amer. Meteor. Soc.*, **93**, 485–498

Thompson, D. W. J., J. M. Wallace, and G. C. Hegerl, 2000: Annular Modes in the Extratropical Circulation. Part II: Trends. *J. Clim.*, **13**, 1018–1036, https://doi.org/10.1175/1520-0442(2000)013<1018:AMITEC>2.0.CO;2.

Thompson, D. W., S. Solomon, P. J. Kushner, M. H. England, K. M. Grise, and D. J. Karoly, 2011: Signatures of the Antarctic ozone hole in Southern Hemisphere surface climate change. *Nature Geoscience*, **4,** 741-749.

Trenberth, K., 1991: Storm Tracks in the Southern Hemisphere. *J. of Atmos Sciences*. **48**, 2159–2178 DOI: https://doi.org/10.1175/1520-0469(1991)048

Trenberth, K. E., and J. T. Fasullo, 2013: An apparent hiatus in global warming? *Earths Future*, **1**, 19–32, https://doi.org/10.1002/2013EF000165.

——, ——, G. Branstator, and A. S. Phillips, 2014: Seasonal aspects of the recent pause in surface warming. *Nat. Clim. Change*, **4**, 911–916,.

Turner, J., T. Phillips, J. S. Hosking, G. J. Marshall, and A. Orr, 2013: The Amundsen Sea low. *Int. J. Climatol.*, **33**, 1818–1829, https://doi.org/10.1002/joc.3558.

Turner, J., G.J. Marshall, K. Clem, S. Colwell, T. Phillips, H. Lu, 2019: Antarctic temperature variability and change from station data. *International Journal of Climatology*. In press.

Vuille, M., E. Franquist, R. Garreaud, W. Lavado, C. Bolivar Cáceres, 2015: Impact of the global warming hiatus on Andean temperature. *J. Geophys. Res. Atmos*., **120**, DOI: 10.1002/2015JD023126

Volkov, D., S. Lee, F. Landerer and R. Lumpkin, 2017: Decade-long deep-ocean warming detected in the subtropical South Pacific. *Geophys. Res. Lett.*, **44**, 927–936

Xie, P., and P.A. Arkin, 1997: Global precipitation: A 17-year monthly analysis based on gauge observations, satellite estimates, and numerical model outputs. Bull. Amer. Meteor. Soc., 78, 2539 - 2558.

Yiu, Y. Y. S., and A. C. Maycock, 2019: On the seasonality of the El Niño teleconnection to the Amundsen Sea region. *J. Clim.*, https://doi.org/10.1175/JCLI-D-18-0813.1.

You, Y. and J. Furtado, 2017: The role of South Pacific atmospheric variability in the development of different types of ENSO. *Geophys. Res. Lett.*, **44**, 7438–7446

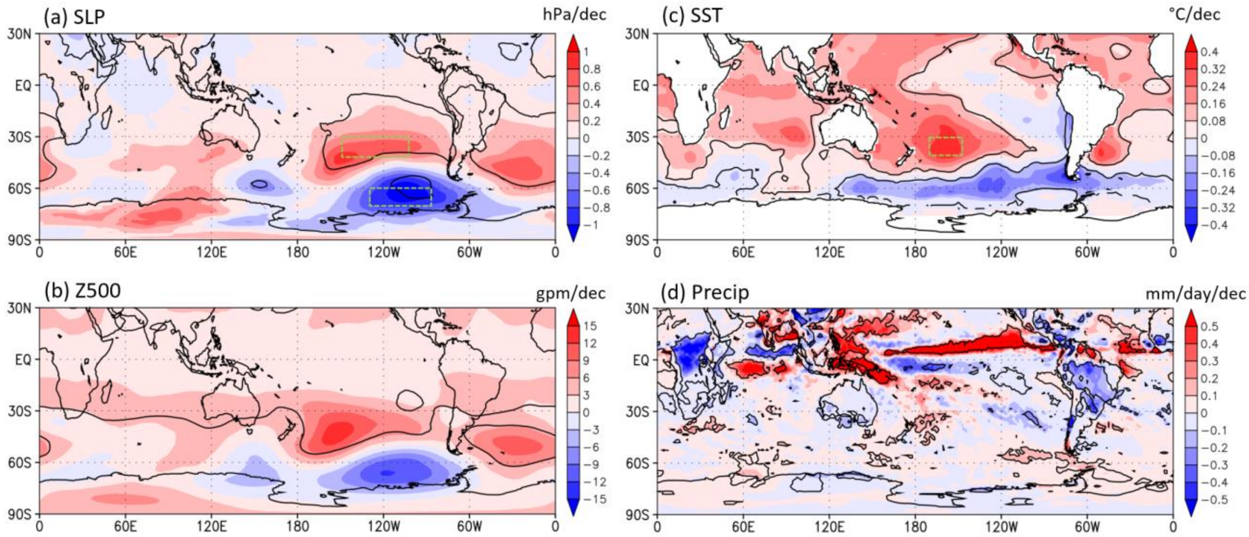

Figure 1. Austral winter (May-September) four-decade trends (1979-2018) of selected fields: (a) Sea level pressure, (b) 500 hPa geopotential height, (c) Sea surface temperature, (d) Precipitation. All data from ERA5 except SST (ERSSTv5). The black contour outlines areas with trends statistically significant (*p*<0.10). Green boxes in (a) outline the regions to define the pressure dipole and (c) the Subtropical South West Pacific (SSWP).

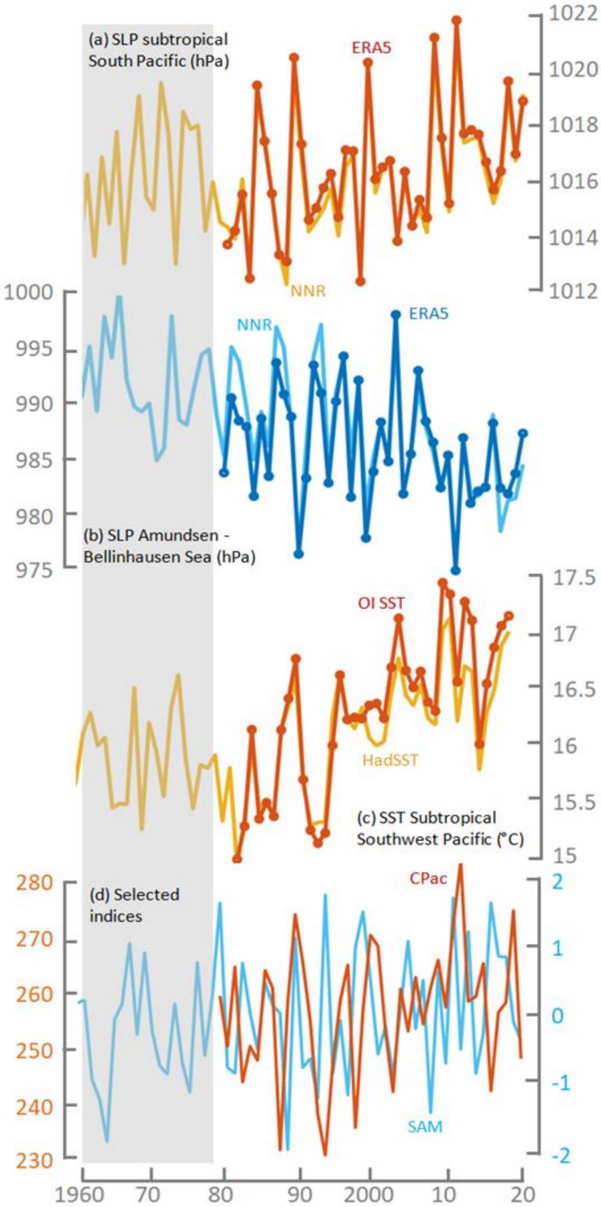

Figure 2. Time series of austral winter (May-September) mean of selected variables. From top to bottom: SLP over the subtropical south Pacific (40-30°S, 210-260°E), SLP over the Amundsen-Bellingshausen Sea region (70-60°S, 230-280°E), SST over the subtropical southwest Pacific (40-30°S 190-210°E), the CPac index (OLR 15°S-Eq, 170-192°E) and the (Marshall 2003) SAM index. The gray box emphasizes the period used to calculate trends (1979-2018). Data source indicated in each graph.

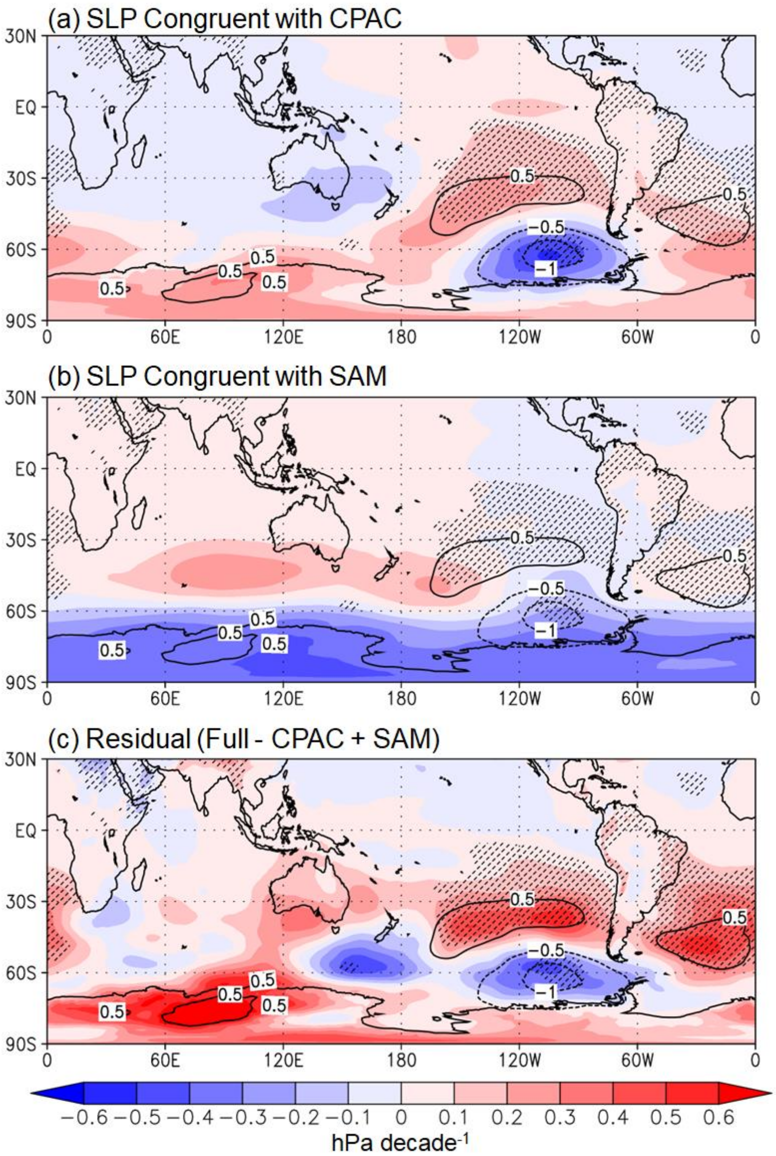

Figure 3. (a) Austral winter (May-September) four-decade trends (1979-2018) of SLP that are linearly congruent with the Central Pacific drying (CPac; see details in section 3a). (b) As panel (a) but for SLP trends that are linearly congruent with the SAM. (c) Difference between the full trends (cf. Fig. 1a) and the sum of (a) and (b). For reference, in all panels stippling denotes where the *observed* trends are statistically significant at p<0.10, and the black contours show the *observed* ± 0.5 and 1.0 hPa/dec SLP trends (cf. Fig. 1a).

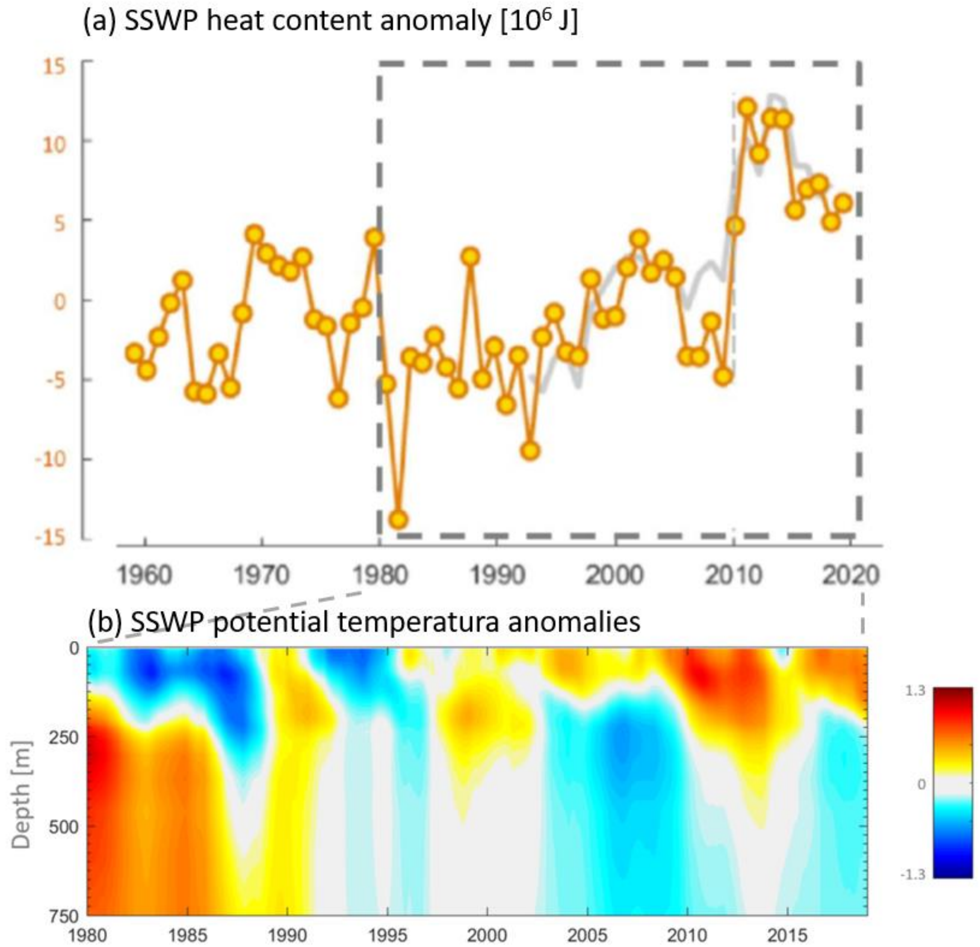

Figure 4. (a) Annual values of ocean heat content anomaly (0-700 m) in the subtropical southwest Pacific (40-30°S 190-210°E). (b) Monthly anomalies (departure from 1980-2000 mean) of ocean potential temperature in the SSWP. Data from NCEP-GODAS.

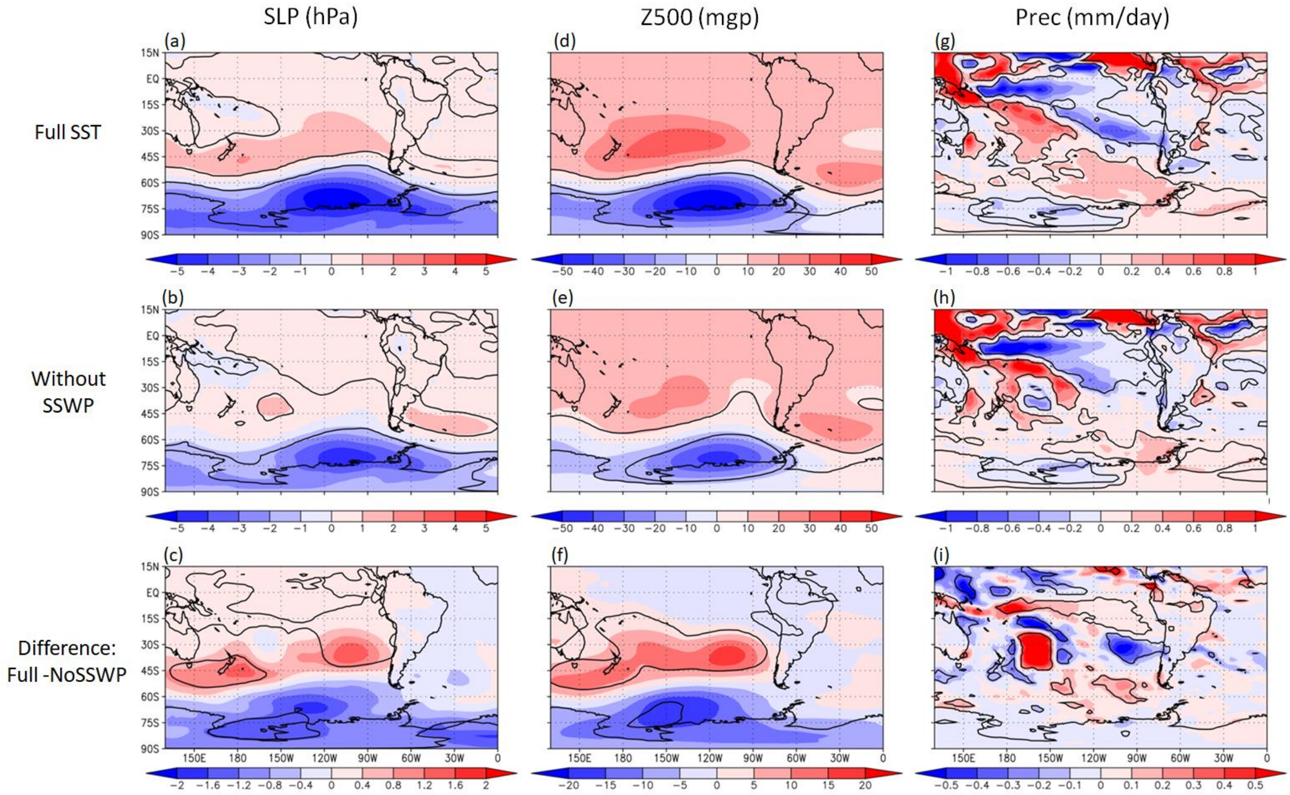

Figure 5. Results from CESM sensitivity experiments (see details in section 2b). Upper row: Difference between CLIM+dSST and CLIM runs showing the atmospheric response to the observed SST change between 1979 and 2018. The atmospheric fields are SLP (left panel), 500 hPa geopotential (central panel) and total precipitation (right panel). Middle row: As in upper row but for the difference between CLIM+dSST without the SSWP warming and CLIM. Lower panel: Difference between CLIM+dSST and CLIM+dSST without the SSWP, thus revealing the direct atmospheric response to the subtropical southwest Pacific warming. The black contour outlines where the differences between each group following a two-tailed *t* test (58 degrees of freedom) are statistically significant at $p<0.10$.

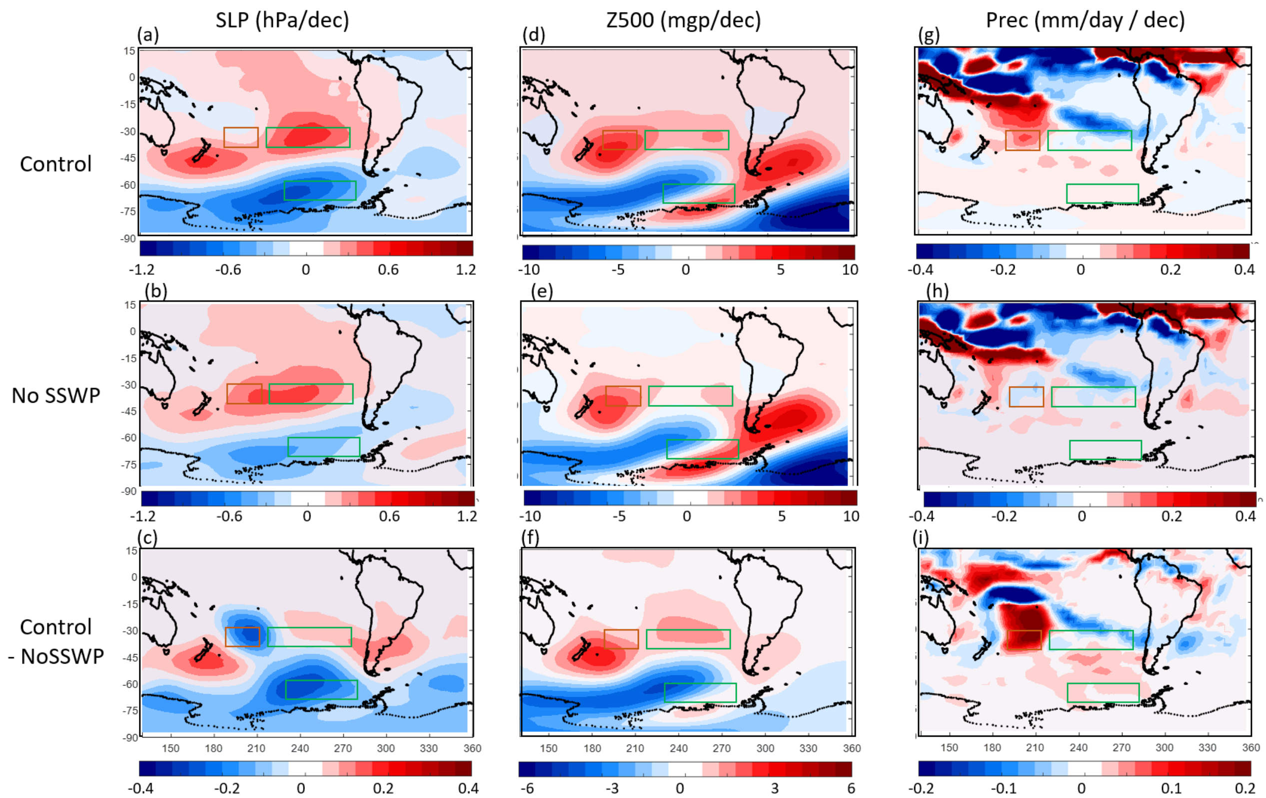

Figure 6. Results from SPEEDY sensitivity experiments (see details in section 2c). Upper row: Winter (MJJAS) trends from 1977 to 2016 simulated by the model forced by observed SST over the whole globe (Control). The atmospheric fields are SLP (left panel), 500 hPa geopotential (central panel) and total precipitation (right panel). Middle row: As in upper row but for the experiment in which the model was forced by observed SST except over the SSWP (No SSWP warming). Lower panel: Difference between Control minus No-SSWP warming trends, thus revealing the direct atmospheric response to the subtropical southwest Pacific warming (shown by the orange box). The ABS region and subtropical Pacific are outlined by the green box. Significance of the trends in these regions is shown in Sup. Fig. 8.

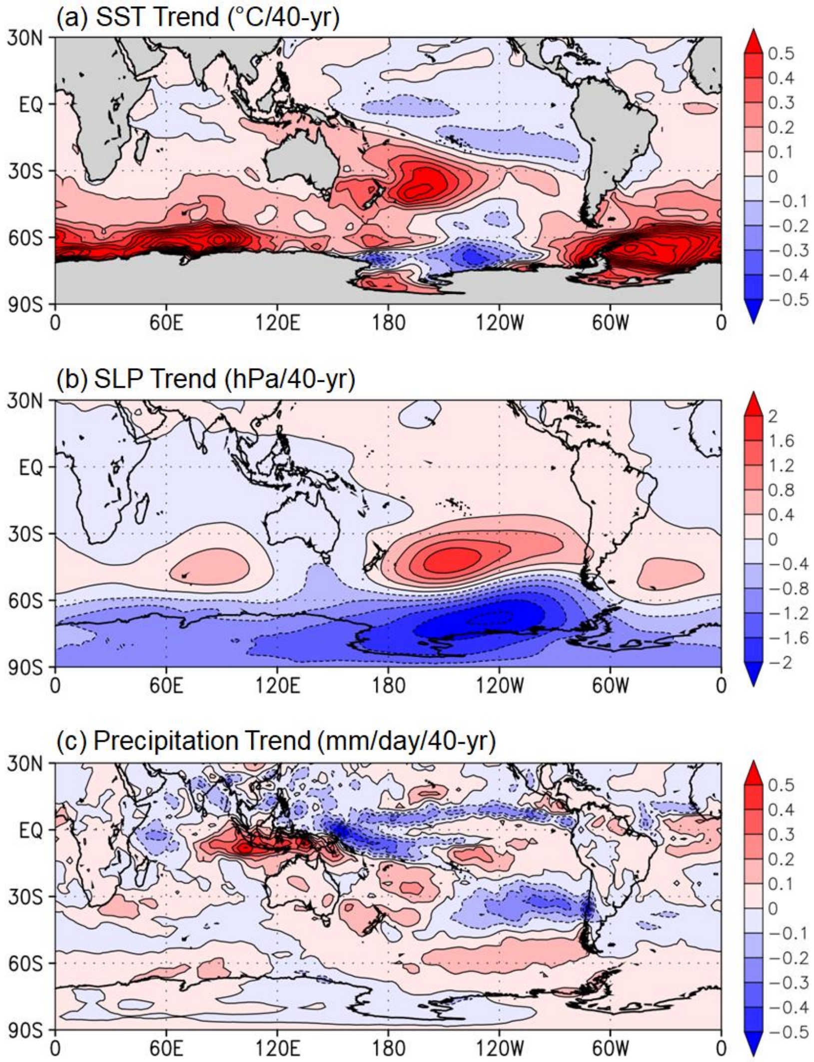

Figure 7. Composite of 40-year trends for highest 40-year warming trend periods over the SSWP (40-30°S 190-210°E) during austral winter obtained from 51 preindustrial fully coupled simulations. The composite maps are (a) SST, (b) SLP and (c) total precipitation.

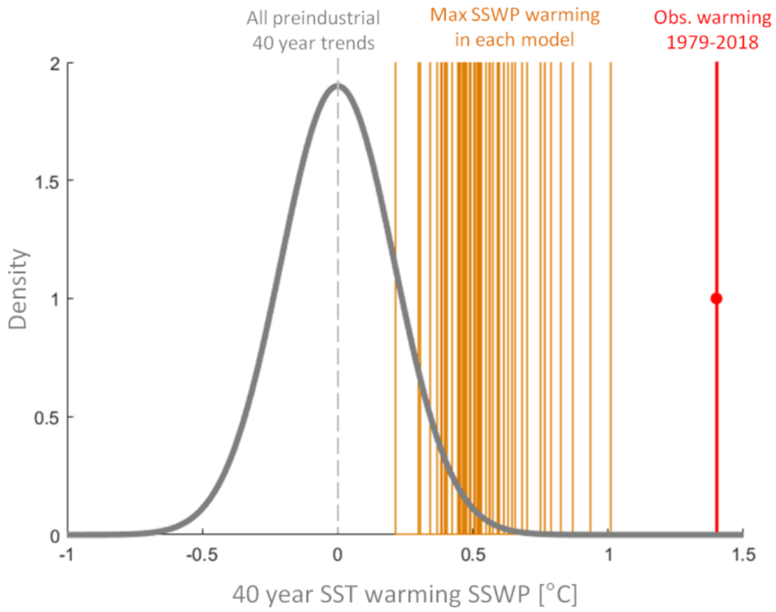

Figure 8. Frequency distribution of all 40-year SST trends over the SSWP (40-30°S 190-210°E) obtained from 51 preindustrial fully coupled simulations (grey curve). The orange vertical lines show the highest 40-year SSWP warming trends in each simulation. The red vertical line shows the observed trend (1979-2018).

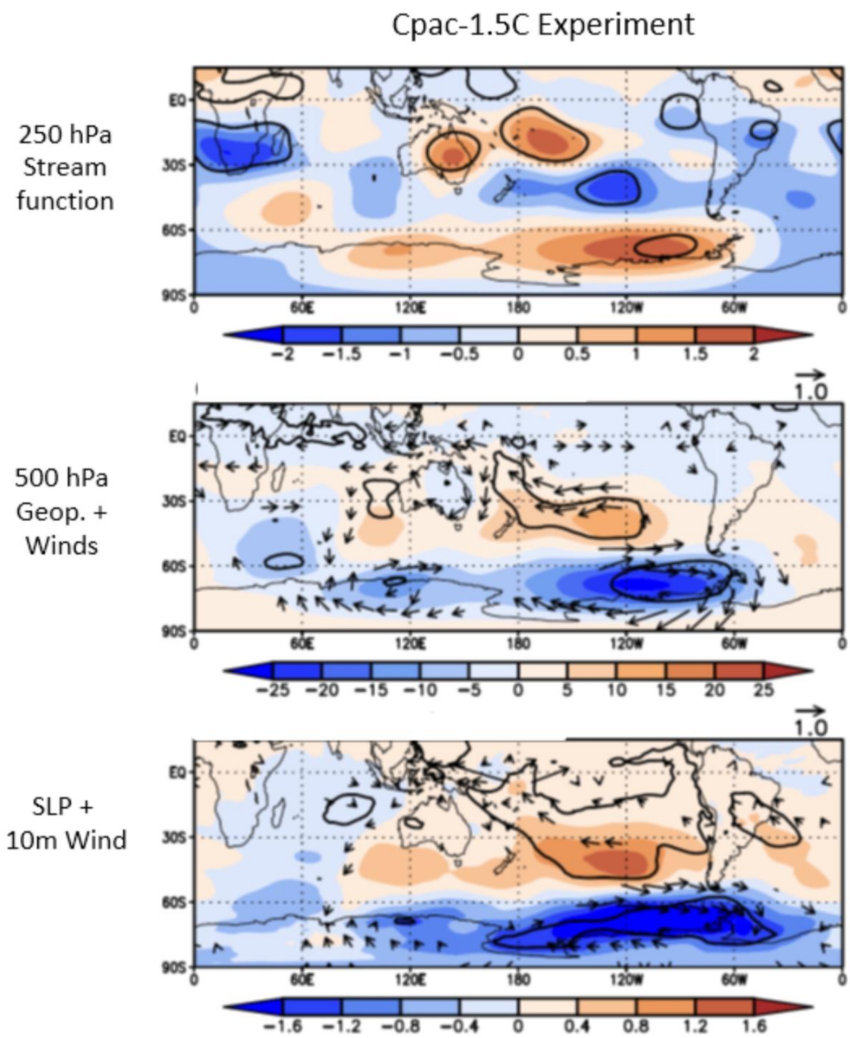

Figure 9. CESM results from the CPac sensitivity experiment in which we imposed a cooling of 1.5ºC in the Central equatorial Pacific (see section 2b for details). The maps show the 30-year average difference between the CPac experiment and the control experiment (climatological SST). The fields are 250 hPa streamfuction (upper panel), 500 hPa geopotential height and winds (middle panel) and sea level pressure and 10-m winds (lower panel).

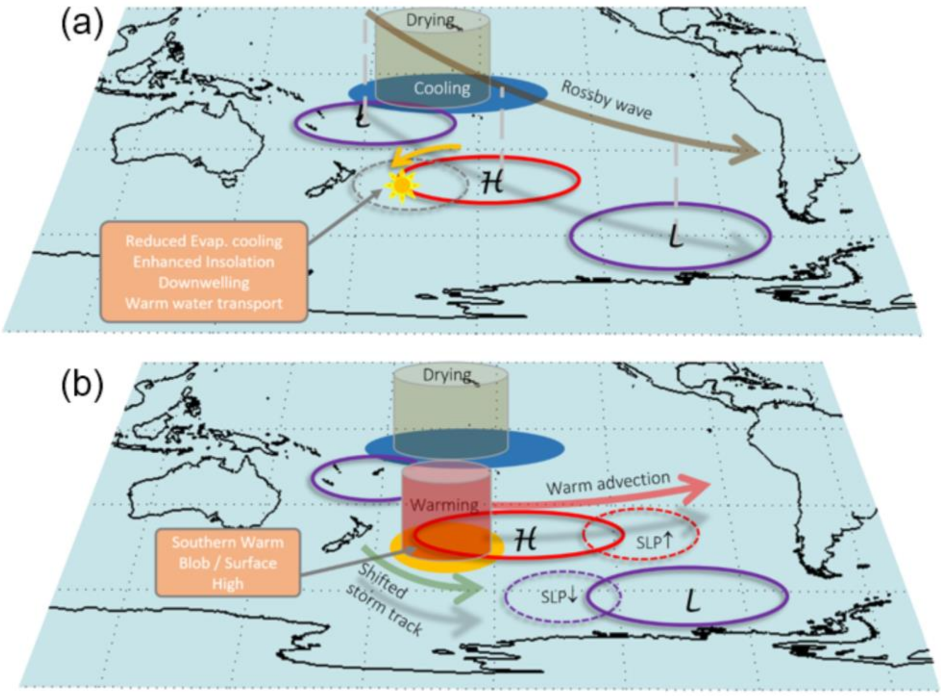

Figure 10. Schematic conceptual model of the (a) initiation and (b) mature phase of the Southern Blob and its effect on the South Pacific atmospheric circulation. The filled blue and yellow ovals indicate sea surface cooling and warming, respectively. The open red and purple ovals indicate positive and negative pressure anomalies, respectively. Other symbols labeled in the Figure. See section 5 for a full discussion.

Tables

Table 1. Summary of (a) CESM and (b) SPEEDY modeling experiments.

a CESM: In each case we performed a 30-year simulation (following a one-year spin-up) forced by repeating monthly climatologies of SST as described below. In all cases we used GHG and O3 representative of 1850s and repeating monthly climatologies of SIC (see section 2b for details). See Sup. Fig. 1 for the SST boundary conditions.

	Sea surface temperature		
Experiment	SSWP	CPAC	rest of the global ocean
CLIM	Perpetual monthly climatology (1950-2017)		
CLIM+dSST	Perpetual monthly climatology plus total change 1979-2018		
CLIM+dSST No SSWP	Perpetual monthly climatology	Perpetual monthly climatology plus total change 1979-2018	
CPac drying	Perpetual monthly climatology	Perpetual monthly climatology -1.5°C	Perpetual monthly climatology

b. SPEEDY: In each case we performed 50 runs (ensemble members) spanning from 1960 to 2016 (trends were later calculated from 1977 to 2016). The runs differ by slightly different initial conditions. In all cases we use GHG and O3 representative of 1850s.

Experiment	SST over the SSWP	SST over the rest of global ocean
Control	Observed (HadISST) monthly values (from Jan 1960 to Dec 2016)	
No SSWP	Repeating monthly climatology	Observed (HadISST) monthly values

Table 2. Austral winter (MJJAS) Sea Level Pressure trend (hPa/decade) over the period 1979-2018 from multiple datasets. SEP is the subtropical south Pacific (40-30°S, 210-260°E). ABS is the Amundsen Bellingshausen Sea region (70-60S, 230-280E). In each case we present the mean trend (estimated by least-square fitting) ± its 90% confidence level according to a two-tailed student-t test.

Product	SSEP	ABS	Reference
ERA-Interim	0.72 ± 0.4	-1.09 ± 0.7	Berrisford et al. 2011
NCEP-DOE Rea2	0.71 ± 0.4	-1.66 ± 0.7	Kanamitsu et al. 2002
NCEP-NCAR Rea1	0.68 ± 0.3	-1.99 ± 0.7	Kalnay et al, 1996
ERA-5	0.67 ± 0.4	-1.03 ± 0.7	Hersbach et al. 2019
HadSLP2R	0.55 ± 0.3	-2.17 ± 0.6	Allan and Ansell 2006

Table 3. Interannual correlations of winter mean (MJJAS) time series from 1979 to 2018. Upper part: detrended time series; Lower part: original time series. Significance at p<0.05 (p<0.1) indicated by * (**)

	CPac OLR	SSWP SST	ABS SLP	SSEP SLP	SAM index
CPac OLR	1.	0.67 **	-0.38 *	0.36 *	0.02
SSWP SST	0.59 **	1.	-0.31 *	0.24	0.04
ABS SLP	-0.43 *	-0.40 *	1.	-0.52 *	-0.62 **
SSEP SLP	0.41 *	0.42 *	-0.56 *	1.	0.09
SAM index	0.03	0.16	-0.63 **	0.14	1.

Table 4. Austral winter (MJJAS) Sea Surface Temperature trend (°C/decade) over the period 1979-2018 (except for OISST V2: 1982-2018) from multiple datasets over the Subtropical Southwest Pacific (40-30°S, 190-210°E). In each case we present the mean trend (estimated by least-square fitting) ± its 90% confidence level according to a two-tailed student-*t* test.

Product	SSEP	Reference
ERSST V5	0.35 ± 0.05	Huang et al. 2014
COBE SST2	0.36 ± 0.06	Hirahara et al. 2014
HadISST1	0.25 ± 0.06	Rayner et al. 2003
OISST V2*	0.34 ± 0.08	Reynolds et al. 2003.